Composites Part B 223 (2021) 109128

Contents lists available at ScienceDirect

Composites Part B

journal homepage: www.elsevier.com/locate/compositesb

Novel computational design of high refractive index nanocomposites and effective refractive index tuning based on nanoparticle morphology effect

Sipan Liu [a], Md Didarul Islam [a], Zahyun Ku [b,**], Darryl A. Boyd [c,***], Yaxu Zhong [d], Augustine M. Urbas [b], Evan Smith [e], John Derov [f], Vinh Q. Nguyen [c], Woohong Kim [c], Jasbinder S. Sanghera [c], Yeongun Ko [g], Jan Genzer [g], Xingchen Ye [d], Zhanhu Guo [h], Eunice Seo [a], Jong E. Ryu [a,*]

[a] Department of Mechanical and Aerospace Engineering, North Carolina State University, 1840 Entrepreneur Drive, Raleigh, NC, 27695, USA
[b] Materials and Manufacturing Directorate, Air Force Research Laboratory, WPAFB, OH, 45433, USA
[c] Optical Sciences Division, Naval Research Laboratory, 4555 Overlook Avenue SW, Washington, D.C, 20375, USA
[d] Department of Chemistry, Indiana University, 800 E. Kirkwood Ave, Bloomington, IN, 47405, USA
[e] KBR, Inc., 2601 Mission Point Blvd., Beavercreek, OH, 45431, USA
[f] Sensors Directorate, Air Force Research Laboratory, WPAFB, OH, 45433, USA
[g] Department of Chemical and Biomolecular Engineering, North Carolina State University, 911 Partners Way, Raleigh, NC, 27695, USA
[h] Department of Chemical and Biomolecular Engineering, University of Tennessee, Knoxville, TN, 37996, USA

ARTICLE INFO

Keywords:
Polymer-matrix composites (PMCs)
Optical properties
Finite element analysis (FEA)
Physical methods of analysis

ABSTRACT

This study introduces a method to predict the refractive index (RI) of nanocomposites with the Finite Elements Analysis (FEA) based on the Fabry-Pérot interference. The efficacy was verified by comparing the estimated composites' RI with the available data in the literature. In the experimental verification, the FEA-based prediction showed closer results with the measurement as compared to the effective medium approximation (EMA) approaches, which are prevalently used to predict the physical properties of nanocomposites. Due to the modeling capability, the FEA-method could investigate the effect of the nanoparticle morphology (particle size, shape, and orientation) and distribution. Large particle size, particle agglomeration in high electric-field amplitude region, and particle elongation along the light oscillating direction are found to be the major factors to enhance the RI of composites. The underlying mechanism of RI changing is attributed to the light scattering by embedded nanoparticles, which provides one potential real-time RI tuning schematic.

1. Introduction

Polymers have been widely used as optical components in a variety of settings, such as the micro-lens array on image sensors [1,2], anti-reflection films [3], lenses [4], and polarizers [5,6], which are produced by facile coating or molding methods due to the processibility of polymers. Polymers are inexpensive, lightweight, and easy to process compared to inorganic materials of the functional counterparts [7–9]. However, some intrinsic limitations of polymers, including low refractive index (RI), spectral absorption, and thermal degradation, remain challenges in designing optical devices with tuned optical polymers [8,10–16]. For those reasons, reinforcing the deficient physical properties has been a significant effort in photonics and optics research with polymers [2,17–22].

Moieties with high molecular polarizability, such as chalcogenide [23–25], phosphorus [26,27], halogen-element [28], and organometal [29–32], were incorporated into the polymers to adjust the RI. For example, the RI of poly(sulfur-random-1,3-diisopropenylbenzene) (poly (S-*r*-DIB)) was increased from 1.765 to 1.865 at the wavelength of 633 nm as the weight fraction of the chalcogenide (S) varied from 50% to

* Corresponding author.
** Corresponding author.
*** Corresponding author.
E-mail addresses: zahyun.ku.1.ctr@us.af.mil (Z. Ku), darryl.boyd@nrl.navy.mil (D.A. Boyd), jryu@ncsu.edu (J.E. Ryu).

https://doi.org/10.1016/j.compositesb.2021.109128
Received 23 March 2021; Received in revised form 2 July 2021; Accepted 5 July 2021
Available online 7 July 2021
1359-8368/© 2021 Elsevier Ltd. All rights reserved.

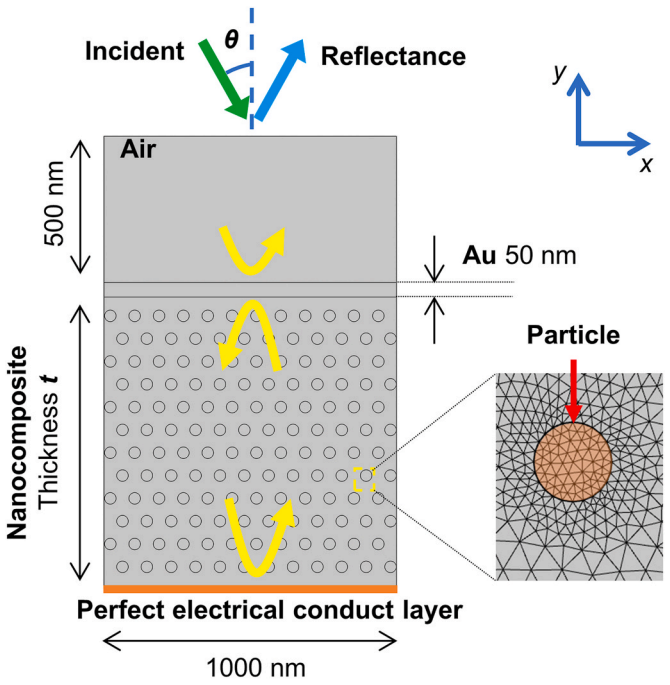

Fig. 1. 2-dimensional (2D) FEA-based simulation model for the optical cavity made from the nanocomposite. Nanoparticles are assumed to be evenly dispersed in the polymer matrix.

70% [25]. Olshavsky et al. synthesized a series of polyphosphazenes with organic side groups containing halogen-elements (Br or I) to tune the RI ranging from 1.60 to 1.75 at the wavelength of 550 nm [26]. An organometallic hyperbranched polydiyne, poly[tris(4-ethynylphenyl)-amine](Co) (hb-PTEPA(Co)), showed the refractive index as high as 1.813–1.713 at the wavelength of 600–1700 nm [29]. However, the modification of a polymer chemical structure by substituting with the high polarizability moieties often deteriorates the structure stability. It thus results in the lower glass transition temperature (T_g) and the mechanical modulus [23,25,32]. For instance, although the RI of poly(S-*r*-DIB) can be increased due to changing the sulfur content from 50 wt% to 70 wt%, Young's modulus decreases from 1.21 ± 0.28 GPa to 0.43 ± 0.08 GPa, the tensile strength lowers from 10.1 ± 2.11 MPa to 2.33 ± 0.15 MPa, and the T_g also reduces from 36.5 to 9.9 °C [25].

Inorganic nanoparticles have also been used to reinforce the RI and the thermomechanical stability of optical polymers, while the polymer matrix provides the structural integrity necessary for good processability [33–41]. For example, Islam et al. achieved a simultaneous increase of the RI and the T_g of poly(S-*r*-DIB) from 1.67 to 1.78 (6.58%) and from 9.6 °C to 31.4 °C, respectively, by adding 20 wt% ZnS nanoparticles without an optical transmission loss in the mid-wavelength infrared (MWIR) regime (3–5 μm) [41,42]. In addition, Camenzind et al. obtained a Young's modulus increasing of polydimethylsiloxane (PDMS) from 0.8 MPa to 2.8 MPa by adding 15 vol% silica nanoparticles [43].

The effective medium approximations (EMAs) are the most used design principles of the optical nanocomposites. The representative EMA models, such as the Maxwell-Garnett theory (MGT), Lorenz-Lorentz (L-L), Bruggeman, Parallel, and Drude models, are summarized in Table S1. However, the EMA models are based on only the

Table 1
Summary of the measured RIs (RI_{ref}) reported in the references, FEA-derived RIs (RI_{FEA}), error-corrected RIs (RI_c), and the errors between RI_c and RI_{ref} for the nanocomposites including $BaTiO_3$/PMMA, TiO_2/PMMA, ZnO/PMMA, Nb_2O_5/Cyclomer-P ACA250, and SiO_2/Cyclomer-P ACA250.

Material	Particle f_V	RI_{FEA}	RI_c	RI_{ref}	Error
$BaTiO_3$ (n = 2.4, d = 21 nm)/ PMMA (n = 1.49) [67]	8%	1.588	1.548	1.550	0.16%
	13%	1.625	1.584	1.580	0.26%
	23%	1.700	1.657	1.640	1.05%
	36%	1.795	1.750	1.710	2.33%
	52%	1.941	1.892	1.820	3.97%
TiO_2 (n = 2.76, d = 19 nm)/ PMMA (n = 1.49) [68]	0.6%	1.526	1.488	1.490	0.16%
	1.4%	1.533	1.495	1.496	0.09%
	3%	1.545	1.506	1.507	0.06%
ZnO (n = 2.02, d = 10 nm)/ PMMA (n = 1.49) [69]	1.3%	1.531	1.492	1.492	0.02%
	2.4%	1.536	1.497	1.496	0.06%
	4.7%	1.547	1.508	1.504	0.30%
	7.8%	1.562	1.522	1.507	1.02%
Nb_2O_5 (n = 2.32, d = 15 nm)/ Cyclomer-P (n = 1.51) [70]	7%	1.595	1.555	1.550	0.32%
	18.5%	1.675	1.633	1.625	0.48%
SiO_2 (n = 1.46, d = 15 nm)/ Cyclomer-P (n = 1.51) [70]	4%	1.545	1.506	1.505	0.08%
	14%	1.540	1.502	1.504	0.16%
	28%	1.531	1.492	1.489	0.22%
	48%	1.519	1.481	1.480	0.05%

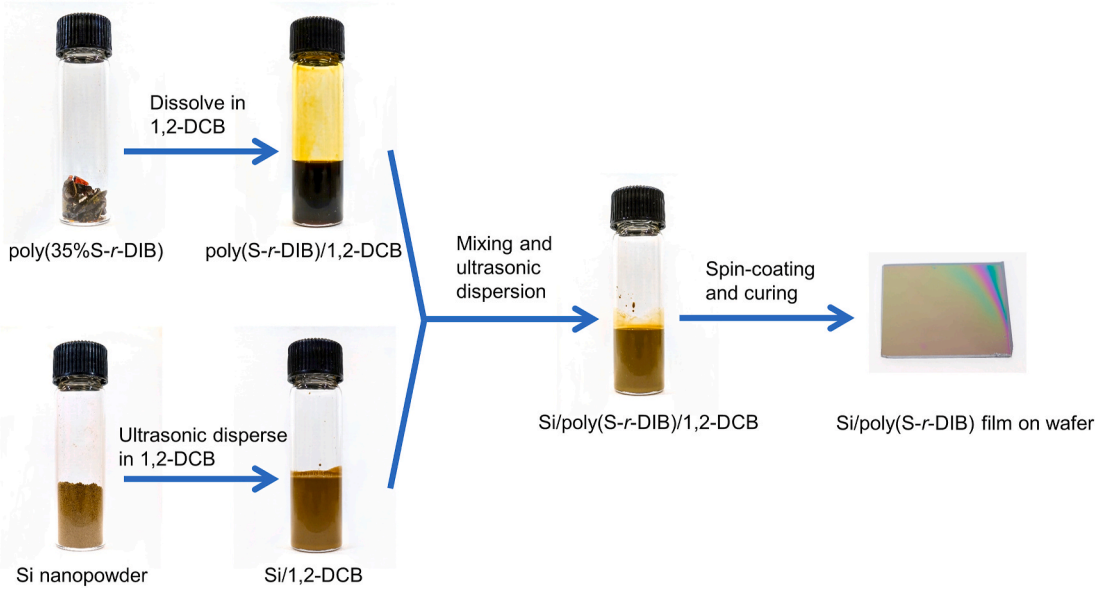

Fig. 2. The fabrication procedure of Si/poly(S-*r*-DIB) polymeric nanocomposite.

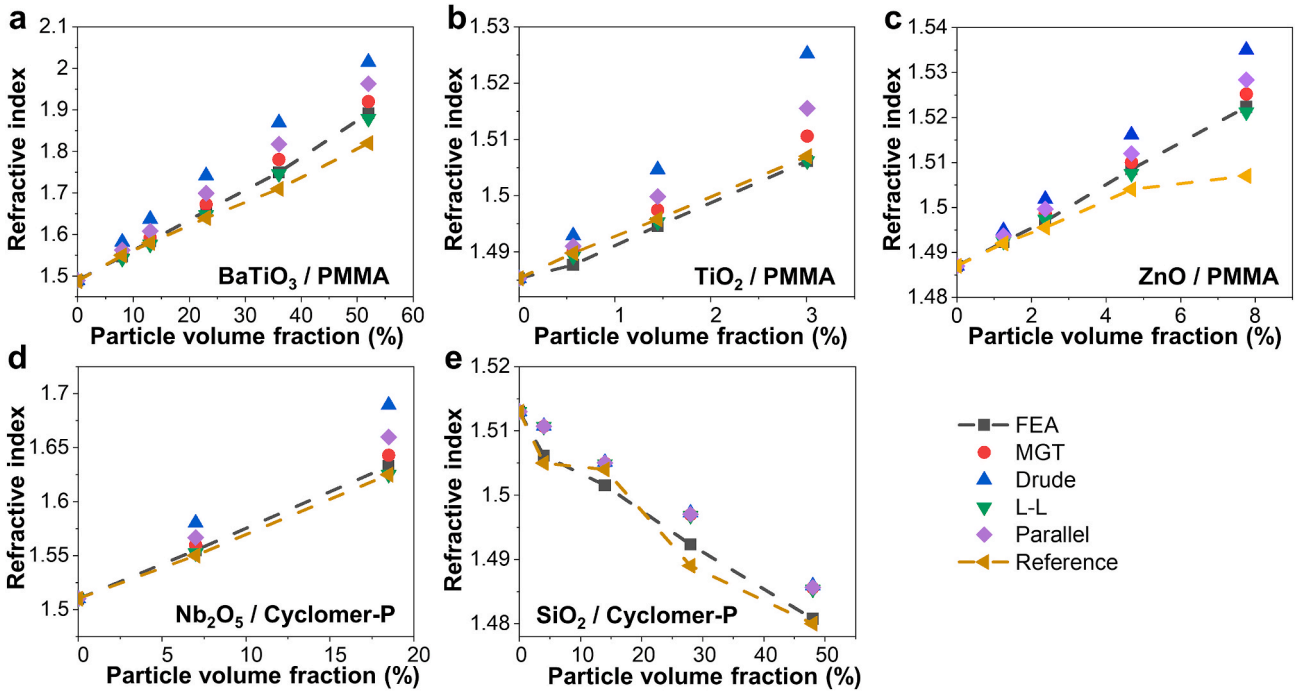

Fig. 3. Comparison of the FEA-based prediction with the reference measurement data [67–70] and the traditional EMA models (Maxwell-Garnett theory (MGT), Lorenz-Lorentz (L-L), Parallel, and Drude) of various nanocomposite systems consisting of (a) $BaTiO_3$/PMMA, (b) TiO_2/PMMA, (c) ZnO/PMMA, (d) Nb_2O_5/Cyclomer-P, and (e) SiO_2/Cyclomer-P.

volume ratio and RIs of the constituent materials [44,45], excluding the effect of the nanoparticle morphology (particle size, shape, and orientation) and the dispersion state. It is often found that there is an apparent discrepancy between experimental results and EMA prediction [44, 46–49]. Further, the choice of an EMA model for a specific composite material system is often arbitrary [44]. Therefore, the best-fitting model for the nanocomposite is to be justified only through experiments.

On the other hand, the effective properties of the composites can be indirectly derived through a physics-based equation interrelating the system responses and stimuli. In this study, we demonstrate a proof-of-concept to predict the RI of nanocomposites from the Fabry-Pérot (F-P) resonance behavior simulated by the finite element analysis (FEA) based on Maxwell's equations. The effective RI of the nanocomposite can be calculated using the F-P resonance wavelength and the composite film thickness [50]. Since both the FEA and effective RI calculation are based on physical principles, the derived RI is expected to be more reliable compared to the EMA models, which simply interpolate the effective property based on the volume ratio between two materials. In addition, the FEA method can evaluate the nanoparticle morphology and spatial distribution through the model design. The objectives of this study are three-fold: firstly, to create a physics-based FEA model to predict the effective RI of nanocomposites, followed by the validation using data reported in the literature; secondly, to fabricate and characterize the MWIR optical nanocomposites with the FEA-based material design-guideline; finally, to elucidate the effect of the nanoparticle morphology and arrangement on the effective RI that are unattainable by the traditional EMA models.

2. Models and method

2.1. Finite element analysis model

The dips in the reflection spectrum (R) appear at the Fabry-Pérot (F-P) interference resonance wavelengths λ_m of the nanocomposite cavity bounded by two closed boundaries as illustrated in Fig. 1, and the effective refractive index (RI) can be described as

$$n = m\lambda_m / 2t\cos\theta \quad (1)$$

where n, t, θ, and m are the effective RI, the thickness of the nanocomposite cavity, the incidence angle, and the integer was referring to the order of the interference fringe, respectively [51–56]. The multiple layers of air, Au, and nanocomposite were modeled with COMSOL Multiphysics using the Wave Optics Module [57]. The incidence angle θ was normal to the top surface in the FEA ($\theta = 0$). Details of the RI calculation procedure based on Equation (1) can be found in the Supplementary Information (Fig. S1).

Due to the intensive computational cost of 3-dimensional (3D) model analysis, the feasibility of using a 2D model was verified by comparing the reflection spectra. As the verification study, $BaTiO_3$ nanoparticle – poly(methyl methacrylate) (PMMA) composites were used in 3D and 2D models. The locations of F-P resonance dips in the simulated reflection spectra using 3D and 2D models were compared, and the differences at the wavelengths of λ_m were negligible ($\Delta\lambda_m \approx 1$ nm). Note that the difference of calculated effective RIs using 3D and 2D models was obtained with 0.1%–0.16%. The detailed optical properties of $BaTiO_3$ particles and PMMA matrix, particle size, the content of particles, and the simulated reflection spectra of the 3D- and 2D-modeled $BaTiO_3$–PMMA composite cavity are provided in the Supplementary Information (Fig. S2 and Table S2). Based on the feasibility test, 2D models were used in all subsequent simulations.

The layer of Au placed on top of nanocomposite cavity was used as the closed boundary, and its thickness was chosen to be 50 nm for a high Q factor, as a measure of the sharpness of F-P resonance. The preliminary results are shown in Figs. S3–S4 and Table S3. The complex refractive indices of Au and Air were taken from data of Ordal et al. [50] and Ciddor [51], respectively. The closed boundary at the bottom of nanocomposite cavity system was set as a perfect electric conductor (PEC) which is equivalent to a perfect metal so that the perfect reflection and no phase loss are achieved. Additionally, the periodic boundary condition was set at the vertical sides (parallel to y-direction) of unit cell, and x-polarized light (TM-polarized light) was incident along the normal

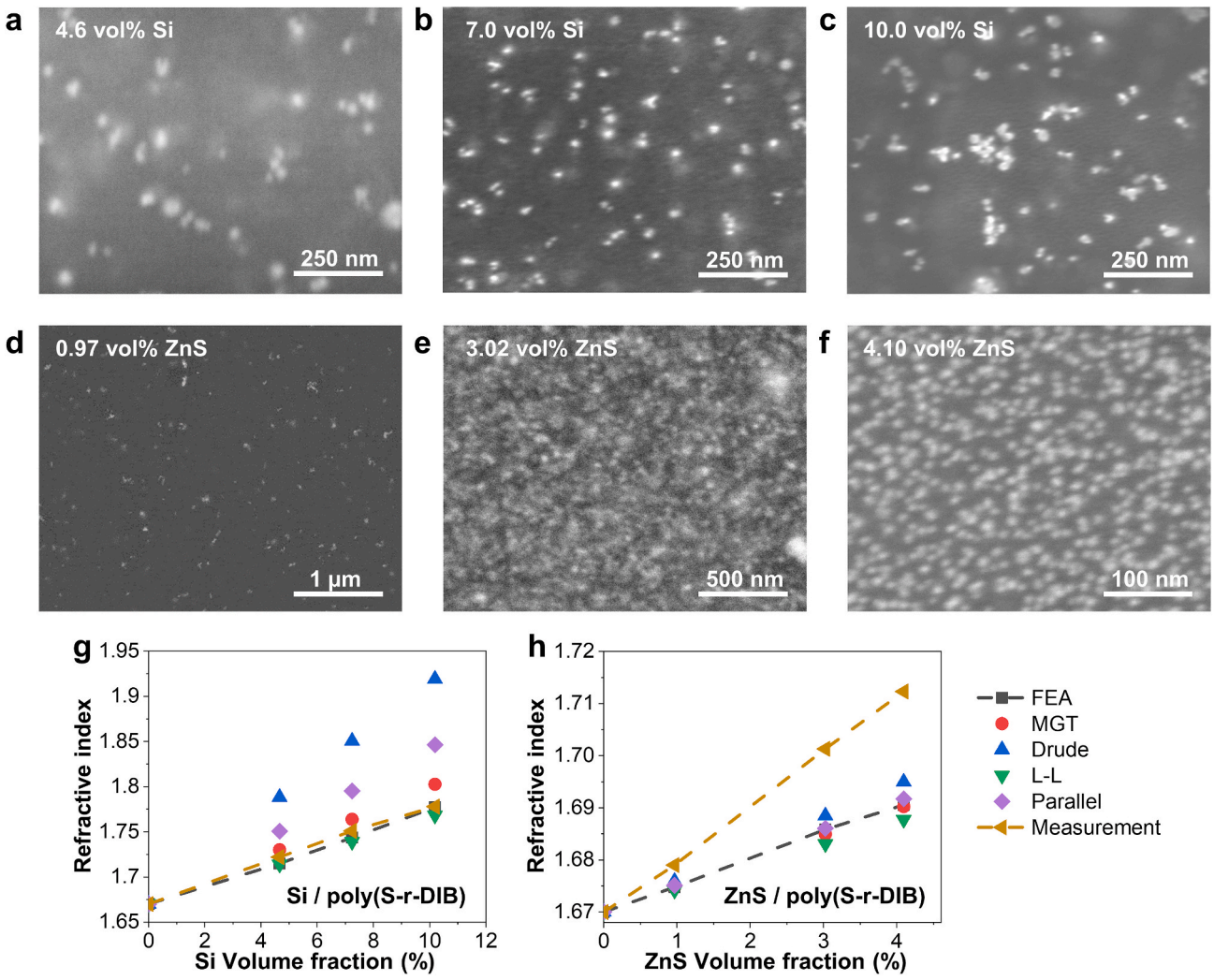

Fig. 4. The surface SEM images (top view) of ORMOCHALC nanocomposites samples. (a–c) Si/poly(S-*r*-DIB) with 4.6, 7, and 10 vol% nanoparticles. (d–f) ZnS/poly (S-*r*-DIB) with 0.97, 3.02, and 4.10 vol% nanoparticles. (g–h) RI_c (labeled as FEA), RI calculated using the traditional EMA models, and the IR-VASE measured RI as a function of Si and ZnS particle volume fractions.

Table 2
Summary of the ellipsometry-measured RI (RI_{EM}), FEA-derived RI (RI_{FEA}), error-corrected RI (RI_c), and the error between RI_c and RI_{EM} of ORMOCHALC nanocomposites.

Particle	Particle f_V	RI_{EM}	RI_{FEA}	RI_c	Error
Si	4.66%	1.722	1.754	1.720	0.14%
	7.24%	1.751	1.783	1.748	0.17%
	10.19%	1.778	1.817	1.782	0.21%
ZnS	0.97%	1.679	1.708	1.675	0.25%
	3.02%	1.701	1.720	1.686	0.91%
	4.10%	1.712	1.724	1.691	1.27%

direction (*y*-direction) as shown in Fig. 1. The thickness of the nanocomposite cavity was selected to be much larger than the size of nanoparticles (~30 times) to ensure homogenous dispersion conditions [58,59].

This FEA model has an intrinsic error which is attributed to the loss by the 50-nm Au layer on top of the cavity. To evaluate this error, a model was computed with the known input RI (RI_{IN}) in the pure polymer cavity, and the computation result, FEA-derived RI (RI_{FEA}), was compared with RI_{IN}. The FEA-simulations were performed with the polymer cavity thickness (1, 1.15, 3 μm), and various values of input RIs ranging from 1.5 to 2 with a step of 0.05. The average percentage errors (given by $|(RI_{FEA} - RI_{IN})/RI_{IN}|\cdot 100\%$) were 2.27% (order $m = 1$; standard deviation $\sigma = 0.04\%$) and 2.58% (order $m = 5$; $\sigma = 0.12\%$), 1.99% (order $m = 1$; $\sigma = 0.04\%$), and 0.78% (order $m = 3$; $\sigma = 0.04\%$) for the cavity thicknesses of 1, 1.15, 3 μm, respectively (Fig. S5 and Tables S4–S6). In our further study, the RI_{FEA} obtained from the F-P simulation and Equation (1) were adjusted by using the average percentage errors depending on the thickness of the cavity and the order of F-P resonance. The error-corrected RI (RI_c) is defined as

$$RI_c = RI_{FEA}/(1 + \text{average percentage errors}) \quad (2)$$

2.2. Material and fabrication

It is desirable to minimize the nanoparticle scattering loss to detect the change in the effective RI accurately. Since the Rayleigh scattering is negligible when the nanoparticle diameter is smaller than $\lambda/10$ [58], the composite materials in this study are composed of nanoparticles with 10–15 nm size and characterized in the MWIR regime (λ = 3–5 μm). The nanocomposite samples were fabricated with an organically modified chalcogenide (ORMOCHALC) polymer, (poly(S-*r*-DIB), due to its low absorption-loss in the MWIR. The poly(S-*r*-DIB) (S 35 wt%, 1,3-DIB 65 wt%) was synthesized by the inverse vulcanization method [5–7,23,25,39,41,60], and the procedure is found in the Supplementary Information.

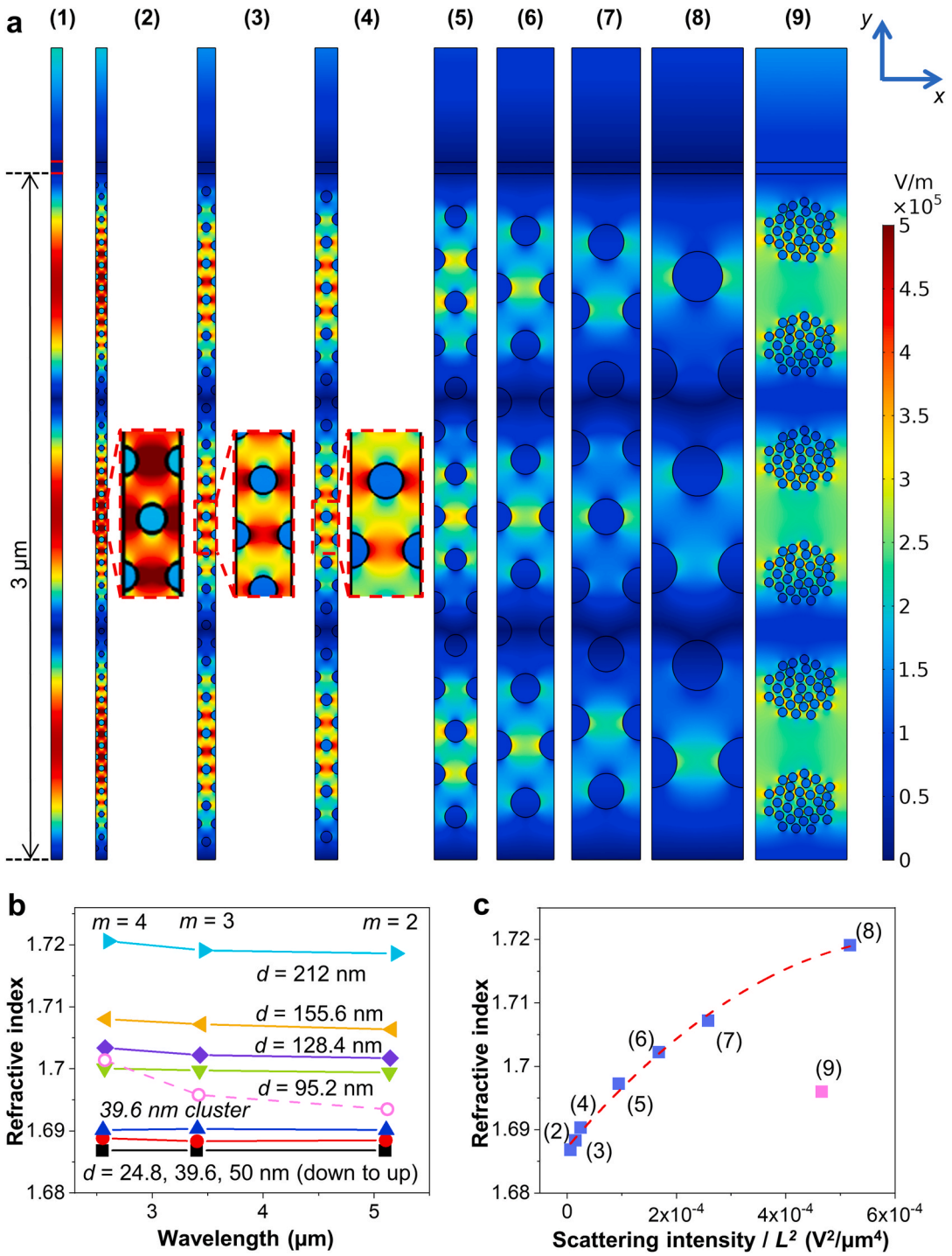

Fig. 5. FEA model for the F-P interference in the nanocomposite cavity depending on the size of embedded nanoparticles. (a) Electric field amplitude in the *x*-direction ($|E_x|$) at the F-P resonance order of 3 ($m = 3$) for embedded particles with diameter of (1) $d = 0$ (no particle), (2) $d = 24.8$ nm, (3) $d = 39.6$ nm, (4) $d = 50$ nm, (5) $d = 95.2$ nm, (6) $d = 128.4$ nm, (7) $d = 155.6$ nm, (8) $d = 212$ nm, (9) 39.6 nm-particle-cluster, effective diameter = 212. (b) The effective RI_c as a function of F-P resonance order (m) and the size of embedded nanoparticles in the nanocomposite cavity. The 39.6 nm-particle-cluster model result is shown as pink dash line. (c) The effective RI_c as a function of the scattering intensity due to the different nanoparticle size embedded in the nanocomposite cavity. (For interpretation of the references to colour in this figure legend, the reader is referred to the Web version of this article.)

Si and ZnS were chosen for the embedded nanoparticles due to the high transmittance and low loss in the MWIR [5,6,61,62]. The nanoparticles are functionalized with the oleic acid capping agent for stable dispersion in the poly(S-*r*-DIB) matrix [41,63,64]. Note that we used the commercial Si nanoparticles in a diameter of 15 nm (US Research Materials, USA), and the synthesized ZnS nanoparticles in an average diameter of 10 nm by the method [41,65,66] as described in the Supplementary Information.

The nanocomposite synthesis procedure is shown in Fig. 2. First, the solid poly(S-*r*-DIB) was ground into powder and dissolved in 1,2-dichlorobenzene (1,2-DCB) solvent in a vial. The mixture was stirred by a magnetic stir-bar for 4 h at 120 °C in an oil bath to dissolve the poly(S-*r*-DIB) in 1,2-DCB completely. Then, the air-cooled solution was filtered by a polytetrafluoroethylene (PTFE) filter with 0.2 μm pore size. The Si

Table 3
Calculation table of the effect of nanoparticle size (d) on the RI of composites, including N (the particle concentration calculated using the fixed particle volume fraction at 19 vol%), $E_{0,NP}$ (electric field amplitude in the particle), σ_{NP} (scattering cross-section area), α_{NP} (the scattering coefficient of nanoparticles), I_{NP} (the scattering loss intensity due to the nanoparticles), and RI_c.

d (nm)	N (μm^{-3})	$E_{0,NP}$ (V/μm)	σ_{NP}/L^2	α_{NP}/L^2 (μm^{-3})	I_{NP}/L^2 ($V^2/\mu m^4$)	RI_c
24.8	19.67	1.23×10^{-1}	6.58×10^{-6}	1.29×10^{-4}	5.88×10^{-6}	1.687
39.6	12.33	9.74×10^{-2}	4.28×10^{-5}	5.27×10^{-4}	1.50×10^{-5}	1.688
50	9.67	8.82×10^{-2}	1.09×10^{-4}	1.05×10^{-3}	2.45×10^{-5}	1.690
95.2	5.00	6.64×10^{-2}	1.43×10^{-3}	7.14×10^{-3}	9.44×10^{-5}	1.697
128.4	3.67	5.68×10^{-2}	4.73×10^{-3}	1.73×10^{-2}	1.68×10^{-4}	1.702
155.6	3.00	5.30×10^{-2}	1.02×10^{-2}	3.06×10^{-2}	2.58×10^{-4}	1.707
212	2.00	4.96×10^{-2}	3.51×10^{-2}	7.03×10^{-2}	5.18×10^{-4}	1.719
39.6-cluster	2.00	4.70×10^{-2}	3.51×10^{-2}	7.03×10^{-2}	4.66×10^{-4}	1.696

and ZnS nanoparticles were dispersed in 1,2-DCB in a separate vial by an ultrasonication probe (1000 W) for 12 h. Finally, the nanoparticle solution (Si or ZnS) was added to the poly(S-*r*-DIB) solution, followed by the sonication for an additional 2 h. The nanocomposite solution (the mixture of the nanoparticle solution and the poly(S-*r*-DIB) solution) was spin-coated on a Si wafer, and cured in a vacuum oven at 80 °C for 2 h. The nanoparticle volume fractions in the composites were 4.6, 7.0, and 10.0 vol% for Si, and 1.0, 3.0, and 4.1 vol% for ZnS.

2.3. Characterization methods

The complex refractive indices of the nanocomposites coated on Si wafers were characterized by using the infrared-variable angle spectroscopic ellipsometer (IR-VASE, Mark II, J. A. Woollam Co.). The IR-VASE measurement procedure is shown in Supplementary information 6.3. The nanoscale surface morphology was observed by scanning electron microscopy (SEM, FEI Verios 460L). The SEM beam conditions were 10 kV, 0.8–1.6 nA, 0V bias and TLD detector with SE mode.

3. Results and discussion

3.1. Model validation

The approach using the FEA-based F-P interference model was validated by reproducing the experimentally measured RIs of nanocomposites reported in literature, including $BaTiO_3$/PMMA [67], TiO_2/PMMA [68], ZnO/PMMA [69], Nb_2O_5/Cyclomer-P ACA250 (Daicel Chemical, Japan) [70], and SiO_2/Cyclomer-P ACA250 [70]. The predicted RI values by the FEA-based F-P interference model were also compared to the traditional EMA models, such as MGT, L-L, Parallel, and Drude models. The input parameters of the FEA models, including the RIs of matrix and particle, the size of particle, and volume fraction, were taken from the literature [67–70], shown in Table 1. It is assumed that the particles are dispersed by equal distance in the matrix polymer in the 2D FEA-model. Since the prism coupling method was used in the references [67–70] to measure the RI at the wavelength of 633 nm, the thickness of the nanocomposite layer t in the FEA model was set as 1 μm to obtain the resonance dips at wavelength ~633 nm. The effective RIs of the nanocomposites are calculated by using Equation (1) based on the resonance wavelength λ_m, the nanocomposite layer thickness t, and the fringe order number m. The resonance wavelengths in the reflection spectra of the nanocomposites are found in Fig. S6. The average percentage error of 2.58%, which corresponds to an error of the 1-μm cavity model at the 5th order resonance (Table S4), was used to correct the FEA-derived RI, i.e., the error-corrected RI as shown in Equation (2). Fig. 3 and Table 1 for the nanocomposites we considered (i.e., $BaTiO_3$/PMMA, TiO_2/PMMA, ZnO/PMMA, Nb_2O_5/Cyclomer-P ACA250, and SiO_2/Cyclomer-P ACA250) illustrate the comparison between the corrected-RIs (RI_c) and the measurement data reported in the references [61–64]. The trend of RI_c agrees well with the measurement data. The largest discrepancy is obtained with 1.05%, 0.16%, 1.02%, 0.48%, and 0.22% for $BaTiO_3$ (excluding the outliers at 36 and 52 vol%), TiO_2, ZnO, Nb_2O_5, and SiO_2 nanocomposites, respectively (Table 1), which is probably due to the non-uniform dispersion and size distribution of the nanoparticles that will be discussed in the following.

3.2. Composite characterization and property prediction

Nanocomposites for MWIR optical devices are designed based on an ORMOCHALC polymer, poly(S-*r*-DIB). The SEM images (top view) of the Si/poly(S-*r*-DIB) composites (Si volume fraction: 4.6, 7.0, and 10 vol%) and the ZnS/poly(S-*r*-DIB) composites (ZnS volume fraction: 0.97, 3.02, 4.10 vol%) show uniform dispersion of particles (Fig. 4(a–f)). The complex refractive index ($n + i \cdot k$) was measured in the wavelength range of 2–6 μm by using the IR-VASE (Fig. S7). Due to the low extinction coefficient of the nanocomposites k at ~4 μm, the nanocomposite thickness t in the FEA model was designed to be 1.15 μm, resulting in the F-P resonance at ~4 μm. The RIs of poly(S-*r*-DIB), Si, and ZnS used in the FEA simulation are fixed at 1.67, 3.4, and 2.3, respectively, according to their RI data at 4 μm [5,71]. The corresponding F-P reflection spectra are shown in the Supplementary Information Fig. S8. The average error of 1.99%, which corresponds to the error of the 1.15-μm cavity model at the 1st order F-P resonance (Table S5), was used to correct the FEA-derived RI using Equation (2). The RI_c matches well with the IR-VASE measurements as summarized in Table 2, and shows comparable or better accuracy as compared to the traditional EMA models (Fig. 4(g–h)). The discrepancy between the predictions and the measurement of ZnS/poly(S-*r*-DIB) is mainly caused by the uncertainties in the composite fabrication, including aggregation and non-uniform morphology of nanoparticles. Compared with the same or higher volume fraction SEM images of Si/poly(S-*r*-DIB), the ZnS/poly(S-*r*-DIB) images showed a denser population of nanoparticles at the top surface of the sample, which indicated that ZnS nanoparticles aggregated on the top surface of the film (further investigation about the uneven distribution was done in the section 3.3.2). Note nanoparticles in FEA-models are evenly distributed with uniform morphology, and the traditional EMA models are only associated with the properties of constituent materials (real and imaginary parts of refractive index of nanoparticle and matrix) and the volume fraction. In the following section, we test the hypothesis that the fabrication uncertainties give rise to the deviation between predicted and measured RIs, which is enabled by using the FEA-based method.

3.3. Effects of composite fabrication uncertainties

3.3.1. Nanoparticle size

The effect of the size of nanoparticles on the composite's effective RI was investigated by the FEA model for the F-P interference in the composite cavity with embedded nanoparticles with diameter (d) of 24.8, 39.6, 50, 95.2, 128.4, 155.6, and 212 nm (Fig. 5(a1-a8)). In addition, to understand the clustering effect, a particle-cluster model was proposed in Fig. 5(a9), where each particle-cluster was constituted by 39.6 nm particles, and the total volume is equal to the model consisting of solid 212-nm particles. The RIs of nanoparticle and polymer matrix were taken as 3.0 and 1.5, respectively. The particles were assumed to be uniformly distributed, and the content of particles was fixed at 19 vol%. The thickness of the composite cavity was 3 μm. The simulated reflectance spectra clearly show the F-P resonance dips corresponding to $m = 4$, 3, and 2 as indicated in Figs. S9(a–c). The average

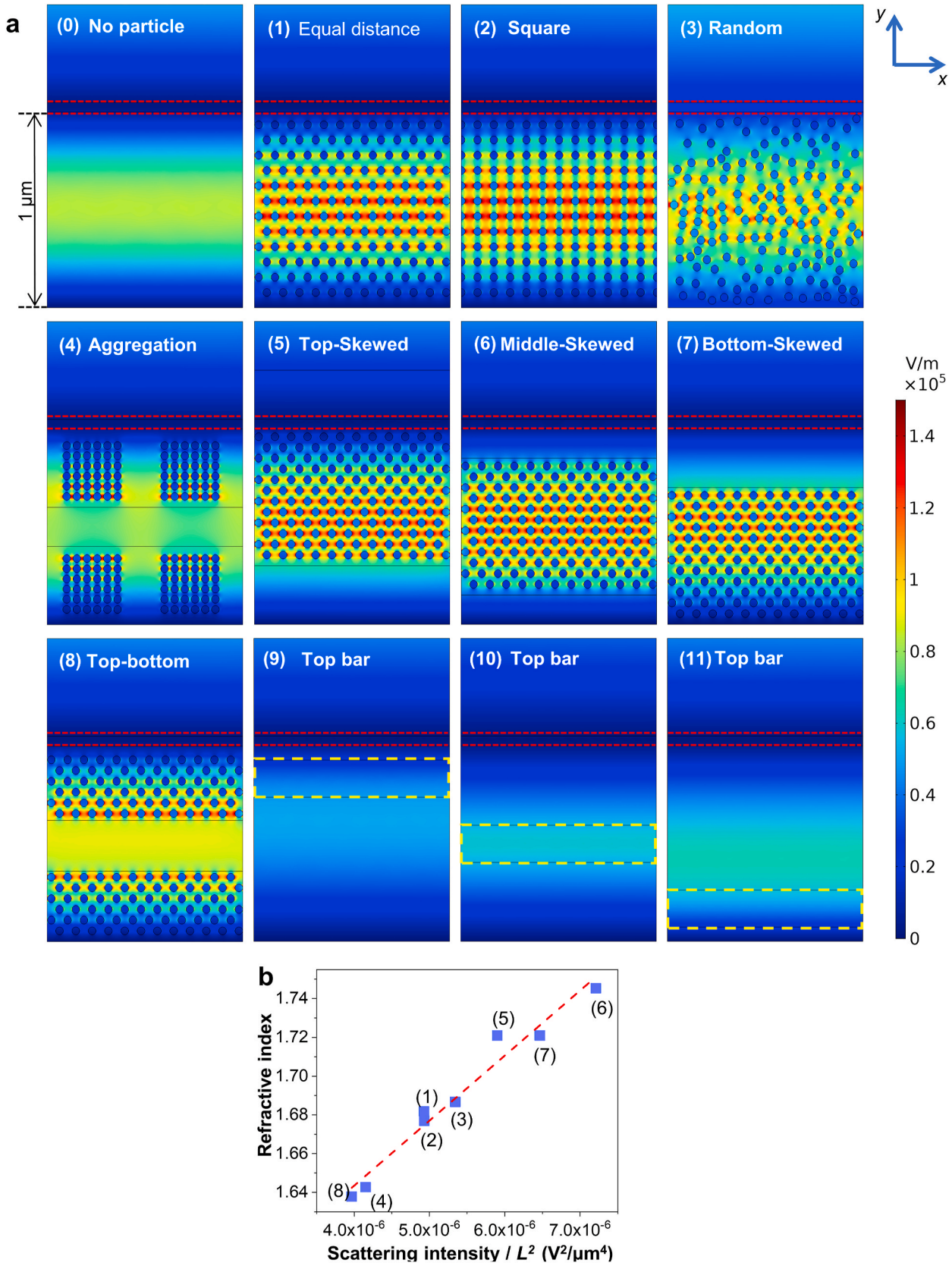

Fig. 6. Effect of nanoparticle arrangement. (a) Electric field amplitude in x-direction ($|E_x|$ at $m = 1$, where λ is ~3.4 μm). The red dash-lines indicate the Au layer atop the nanocomposite cavity, and the yellow dash-lines in a(9)-a(11) indicate the dielectric layers. (b) The effective RI_c as a function of the scattering loss intensity due to different nanoparticle arrangement. (For interpretation of the references to colour in this figure legend, the reader is referred to the Web version of this article.)

Table 4
Calculation table of nanoparticles dispersion state effect on the effective RI, including $E_{0,NP}$ in the *x*-direction, scattering loss intensity I_{NP}, and RI_c.

Dispersion states	$E_{0,NP}$ (V/μm)	I_{NP}/L^2 ($V^2/\mu m^4$)	RI_c
Equal Distance	2.83×10^{-2}	4.93×10^{-6}	1.682
Square	2.83×10^{-2}	4.93×10^{-6}	1.677
Random	2.95×10^{-2}	5.34×10^{-6}	1.687
Aggregation	2.60×10^{-2}	4.15×10^{-6}	1.643
Top-Skewed	3.10×10^{-2}	5.90×10^{-6}	1.721
Middle-Skewed	3.42×10^{-2}	7.21×10^{-6}	1.745
Bottom-Skewed	3.24×10^{-2}	6.47×10^{-6}	1.721
Top-Bottom	2.54×10^{-2}	3.97×10^{-6}	1.638

errors of 0.80%, 0.78%, 0.77%, corresponding to the error of 3-μm cavity model at $m = 4$, 3, and 2, respectively (Tables S6–S8), were used for the error-correction of FEA-derived RIs. As the diameter of particle increases from 24.8 nm to 212 nm, the RI_c also increases from 1.687 to 1.719 ($m = 2$), from 1.687 to 1.719 ($m = 3$), and from 1.687 to 1.721 ($m = 4$), which appear at ~5 μm, ~3.5 μm, and ~2.5 μm, respectively (Fig. 5(b)). The particle-cluster model RIs are 1.694, 1.696, and 1.701 at ~5 μm, ~3.5 μm, and ~2.5 μm, respectively, which are shown as the pink dash line in Fig. 5(b). The RI of the 39.6 nm-particle-cluster model (effective diameter = 212 nm) is significantly lower than the RI of the solid 212-nm model (8) while being still higher than the well-dispersed 39.6 nm model (3).

An increased scattering loss can explain the increase of RI with the particle size by particles [72]. The relationship between the scattering effect and the macroscope RI of the nanocomposite, *n*, can be described as:

$$n - 1 = \frac{\lambda^2}{2\pi}\left(\sqrt{\alpha_{MA} M} + \sqrt{\frac{I_{NP}}{I_0 t}}\right) \tag{3}$$

where λ is the light wavelength, α_{MA} and M are the scattering coefficient and the atomic concentration of the matrix, respectively, I_{NP} is the scattering loss intensity due to the nanoparticles, I_0 is the intensity of the incidence light, and t is the thickness of the composite cavity. Detailed explanation is provided in Section 12 of Supplementary Information. The scattering loss intensity due to nanoparticles embedded in the composite cavity is:

$$I_{NP} \approx \alpha_{NP}\, t \left(E_{0,NP}\right)^2 = N\sigma_{NP}\, t \left(E_{0,NP}\right)^2 \tag{4}$$

where $E_{0,NP}$ is the electric field amplitude calculated by the surface average electric field in the nanoparticles based on the FEA result, N is the particle concentration, σ_{NP} is the scattering cross-section area, and α_{NP} is the scattering coefficient of nanoparticles. Of note, the 2D nanoparticle in the FEA is equivalent to the same diameter cylinder with the unit length L. The scattering cross-section area (σ_{NP}) of cylinder nanoparticles can be calculated by the following equation [73,74]:

$$\sigma_{NP} = \frac{8\pi^3}{3}\frac{V^2}{\lambda^4}\left(n_{particle}^2 - n_{matrix}^2\right)^2 = \frac{\pi^5}{6}\frac{d^4 L^2}{\lambda^4}\left(n_{particle}^2 - n_{matrix}^2\right)^2 \tag{5}$$

where $n_{particle}$ and n_{matrix} are the RIs of nanoparticles and polymer matrix, respectively, d is the particle diameter, and L is the length of cylinder. The RI_c for composites with different nanoparticle sizes are outlined in Table 3. As summarized in Table 3 and Fig. 5(c), we found that the scattering loss intensity I_{NP} and the effective RI increases simultaneously when the nanoparticle size increases (Equations (3)–(5)). For the 39.6 nm-particle-cluster model, the scattering loss intensity I_{NP} is comparable to the solid 212-nm model if the cluster is assumed as a 212-nm solid particle (Table 3), but the effective RI calculated by the FEA model is significantly lower than the solid 212-nm model. This phenomenon demonstrates that the particle cluster cannot provide enough scattering intensity as solid particles, and the data point (9) in Fig. 5(c) actually should shift to the left side near the trend line of solid models.

3.3.2. Particle dispersion

Various particle arrangements, e.g., (1) equal distance, (2) square, (3) random, (4) aggregated, (5) top-skewed, (6) middle-skewed, (7) bottom-skewed, and (8) top-bottom, were FEA-modeled to understand the effect of particle dispersion states on the effective RI of nanocomposites (Fig. 6a). The diameter, RI, and volume fraction of the nanoparticles were 39.6 nm, 3, and 19 vol%, respectively. The RI of polymer matrix was 3, and the thickness of composite cavity (t) was modeled to be 1 μm. The reflectance spectra at ~3.4 μm obtained from the FEA are shown in Fig. S10. The obtained RIc from FEA and Equation (2) are summarized in Table 4. To correct the intrinsic FEA error, the average error, 2.27%, corresponding to the 1-μm cavity model at $m = 1$ (Table S4), was used in Equation (2). In general, the dispersion states with higher particle density within the mid-region in *y*-direction, where the electric field amplitude in *x*-direction is the highest, tend to increase the RI (e.g., (5) top-skewed, (6) middle-skewed, and (7) bottom-skewed) than the states with lower particle density in the mid-region, such as (8), (Fig. 6(a)). This tendency can be interpreted by the nanoparticle scattering loss: for given volume fraction and morphology of particles, the total scattering loss by the nanoparticle I_{NP} increases as more nanoparticles are placed in a region of strong electric field (Equation (4)), finally leading to the increase of RI (Equation (3)), as shown in Fig. 6(b). The scattering loss of nanoparticles I_{NP}/L^2 was calculated by using the surface-average electric field amplitude $E_{0,NP}$ in nanoparticle (Table 4). The scattering coefficient of nanoparticles α_{NP}/L^2 was fixed at 5.27×10^{-4} μm^{-3}. In contrast, when the particles are scarce in the F-P resonance region, such as cases (4) and (8), both I_{NP}/L^2 and effective RI tend to decrease. Moreover, to confirm this conclusion, a dielectric layer of finite thickness (enclosed by yellow dash-lines) with the same RI and volume fraction as the nanoparticles were placed at the top, middle, and bottom in Fig. 6(a9 – a11). The calculated RIs were 2.20, 1.819, and 1.77 for the middle, bottom, and top-located dielectric layers, respectively, which agrees with our expectation that the embedded particles (or dielectric layers) located in the stronger electric field region is more efficient to increase the composite RI.

3.3.3. Shape and orientation effect

The particle shape and orientation effect on the composite RI was studied with the following particle shapes: circle, square, and rectangular (Rec) with aspect ratios (AR) 1:2, 1:3, and 1:5. The square elements have two rotation conditions (refer to *y*-axis): 0° and 45°. Rectangular elements have three rotation conditions: 0°, 45°, and 90°, as shown in Fig. 7(a). The particle volume fraction (19%), material properties (polymer RI = 1.5, particle RI = 3), and the number of particles were kept consistent for all the models (N = 12.33 μm^{-3}). The circle particle diameter was 39.6 nm. The F-P reflection spectra for the composites with those nanoparticles are shown in Fig. S11. The FEA error of 0.78%, which corresponds to the error of the 3-μm cavity model at $m = 3$ (Table S7), was used for the error-correction, and the resultant error-corrected RIs (RI_c) are tabulated in Table 5. It was be found that the elongated particles in the *x*-direction (90° rotation) yield a higher RI, such as Rec AR 1:5 particle with 90° rotation had the largest RI.

The scattering loss by nanoparticles was also used to analyze the relationship between RI increase and different particles' shape and orientation. When the nanoparticle size is small enough compared to the wavelength of incident light (~3.4 μm), the particles' scattering cross-section area and coefficients are independent of the particles' shape and orientation [75]. This conclusion can also be verified by far-field scattering simulation results (Fig. S12 – S13). Thus, the scattering cross-section area of particles σ_{NP} with different shape and orientation could be assumed the same as circular particle with $d = 39.6$ nm, and the scattering coefficient of nanoparticles, α_{NP}/L^2 was fixed at 5.27×10^{-4} μm^{-3}. However, according to Equation (4), the scattering intensity loss I_{NP} also relies on the incident electric field amplitudes $E_{0,NP}$. The incident electric field amplitudes $E_{0,NP}$ could be enhanced due to different shapes

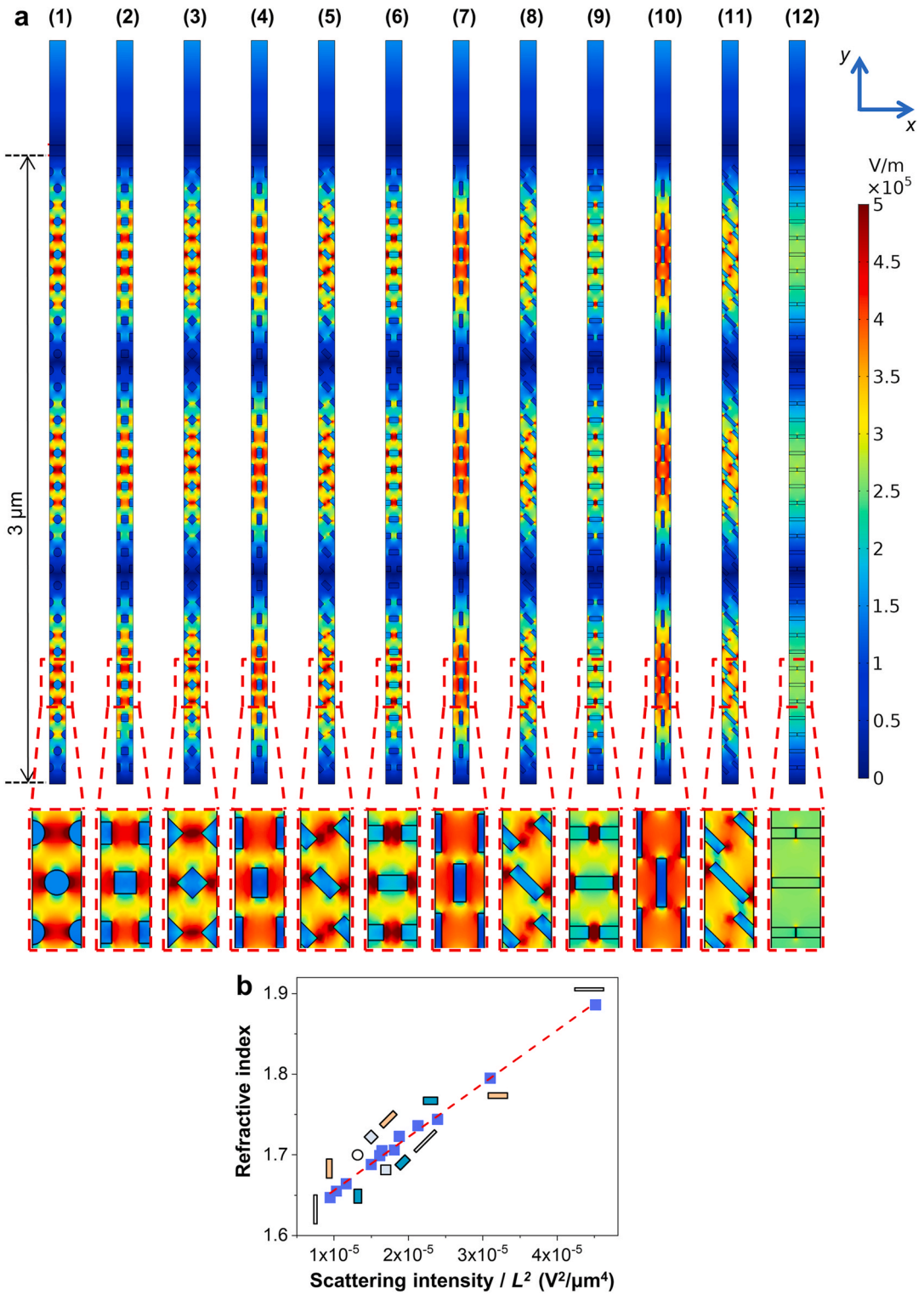

Fig. 7. Particle shape and orientation effect. (a) Electric field map in *x*-direction at the F-P resonance ($m = 3$) for different elements: (1) Circle, (2) Square, (3) Square 45°, (4) Rec 1:2, (5) Rec 1:2 45°, (6) Rec 1:2 90°, (7) Rec 1:3, (8) Rec 1:3 45°, (9) Rec 1:3 90°, (10) Rec 1:5, (11) Rec 1:5 45°, and (12) Rec 1:5 90°. (b) The effective RI_c as a function of the scattering loss intensity due to different nanoparticle shape and orientation.

and orientations particles in the nanocomposite can affect each other and attribute to the different electric field resonance effects [76]. The scattering intensity loss by nanoparticle, I_{NP}/L^2 was calculated by using the surface-average electric field amplitude $E_{0,NP}$ in nanoparticles (Table 5). As the particle elongated in the *x*-direction (light electric field oscillating direction), both $E_{0,NP}$ and I_{NP}/L^2 increase, finally leading to the increase of RI (Fig. 7(b)).

It can be concluded from all particle size, arrangement, and shape effect analyses that the nanoparticles scattering intensity can indicate the composite's effective RI shifting. In all models, higher scattering loss from nanoparticles causes higher effective RI.

Table 5
Calculation table of the particle shape and orientation effect on the RI of composite: E_{MA}, and RI_c.

Model	E_{MA} (V/μm)	I_{NP}/L^2 ($V^2/\mu m^4$)	RI_c
Circle	0.097	1.500×10^{-5}	1.688
Square	0.101	1.613×10^{-5}	1.699
Square 45°	0.102	1.645×10^{-5}	1.705
Rec 1:2	0.086	1.164×10^{-5}	1.664
Rec 1:2 45°	0.107	1.810×10^{-5}	1.706
Rec 1:2 90°	0.123	2.392×10^{-5}	1.744
Rec 1:3	0.081	1.032×10^{-5}	1.655
Rec 1:3 45°	0.109	1.878×10^{-5}	1.723
Rec 1:3 90°	0.140	3.099×10^{-5}	1.795
Rec 1:5	0.077	9.47×10^{-6}	1.647
Rec 1:5 45°	0.116	2.127×10^{-5}	1.736
Rec 1:5 90°	0.169	4.515×10^{-5}	1.886

4. Conclusion

In this paper, we studied the FEA-based RI prediction method for nanocomposite. The method was validated by comparing with the reference data and the fabricated ORMOCHALC composites for MWIR optics. The comparison with the reference data obtained by physical measurement of the samples [67–70], showed that the average error of the RI_c was 0.49%. The causes of the discrepancy between the measurement and the theory-based RI was investigated by varying the particle morphology and dispersion states with the base model composed of the matrix with RI of 1.5 and the nanoparticles with RI of 3 in 19 vol%. When particle size increases from 24.8 nm to 212 nm, the effective RI of nanocomposite also increases from 1.687 to 1.719 due to the scattering loss. The relationship between the scattering loss and the effective RI of nanocomposite was also applied to explain the effect of the particle dispersion state and the particle shape and orientation. The particles arranged in a higher electric field area lead to a higher effective RI. The middle-skewed dispersion (particles aggregated at the high E-field area) and top-bottom dispersion models (particles aggregated at the low E-field area) had the highest and lowest RI as 1.745 and 1.638, respectively, for the study model composite. For different shape and orientation particles, the nanocomposite showed higher effective RI when particle elongation along with electric field oscillation (*x*-direction). When the particle's shape and orientation were AR 1:5 90° (longest side along the *x*-direction) and AR 1:5 elements (shortest side along the *x*-direction), the nanocomposite had the largest RI and smallest RI as 1.886 and 1.647, respectively. It was proved that the scattering loss intensity has a proportional relation with the nanocomposite RI.

Based on this study, future work will entail the quantitative analysis of the nanoparticles morphology effect on the effective RI value of the nanocomposites. Future research also includes optimizing optical and mechanical properties of polymer composites composed of uncertain shape and size particles which is closer to the reality of the composite, and mixed kinds of particles composites system properties characteristic which can be applied on multi-functional composite materials.

CRediT authorship contribution statement

Sipan Liu: Conceptualization, methodology, project administration, data curation, formal analysis, investigation, methodology, software, validation, visualization, writing an original draft, and editing. **Md Didarul Islam:** Data curation, visualization, writing, reviewing, and editing. **Zahyun Ku:** Methodology, software, validation, visualization, supervision. **Darryl A. Boyd:** Resources, supervision. **Yaxu Zhong:** Investigation. **Augustine M. Urbas:** Investigation. **Evan Smith:** Investigation. **John Derov:** Investigation. **Vinh Q. Nguyen:** Investigation. **Woohong Kim:** Investigation. **Jasbinder S. Sanghera:** Investigation. **Yeongun Ko:** Investigation. **Jan Genzer:** Supervision, resources. **Xingchen Ye:** Supervision, resources. **Zhanhu Guo:** Supervision, resources. **Eunice Seo:** Software. **Jong E. Ryu:** Methodology, supervision, project administration, resources, funding acquisition, writing, and editing.

Declaration of competing interest

The authors declare that they have no known competing financial interests or personal relationships that could have appeared to influence the work reported in this paper.

Acknowledgments

S.L., M.D.I., and J.R. were partly supported by North Carolina State University through the new faculty start-up fund; and J.R. was also supported in part by the Air Force Research Laboratory RYDH Sensors Directorate, through the Air Force Office of Scientific Research Summer Faculty Fellowship Program®, Contract Numbers FA8750-15-3-6003 and FA9550-15-0001. This work was performed in part at the Analytical Instrumentation Facility (AIF) at North Carolina State University, which is supported by the State of North Carolina and the National Science Foundation (award number ECCS-2025064). The AIF is a member of the North Carolina Research Triangle Nanotechnology Network (RTNN), a site in the National Nanotechnology Coordinated Infrastructure (NNCI). Y.Z. and X.Y. were supported by the U.S. National Science Foundation (NSF DMR-2102526).

Appendix A. Supplementary data

Supplementary data to this article can be found online at https://doi.org/10.1016/j.compositesb.2021.109128.

References

[1] Regolini JL, Benoit D, Morin P. Passivation issues in active pixel CMOS image sensors. Microelectron Reliab 2007;47:739–42.
[2] Li J, Xu J, Liu X, Zhang T, Lei S, Jiang L, et al. A novel CNTs array-PDMS composite with anisotropic thermal conductivity for optoacoustic transducer applications. Compos B Eng 2020;196:108073. https://doi.org/10.1016/j.compositesb.2020.108073.
[3] Krogman KC, Druffel T, Sunkara MK. Anti-reflective optical coatings incorporating nanoparticles. Nanotechnology 2005;16:S338.
[4] Nakayama N, Hayashi T. Synthesis of novel UV-curable difunctional thiourethane methacrylate and studies on organic–inorganic nanocomposite hard coatings for high refractive index plastic lenses. Prog Org Coating 2008;62:274–84. https://doi.org/10.1016/j.porgcoat.2008.01.002.
[5] Berndt AJ, Hwang J, Islam MD, Sihn A, Urbas AM, Ku Z, et al. Poly (sulfur-random-(1, 3-diisopropenylbenzene)) based mid-wavelength infrared polarizer: optical property experimental and theoretical analysis. Polymer (Guildf) 2019;176:118–26.
[6] Islam MD, Kim JO, Ko Y, Ku Z, Boyd DA, Smith EM, et al. Design of high efficient mid-wavelength infrared polarizer on ORMOCHALC polymer. Macromol Mater Eng 2020;305(5):2000033.
[7] Chung WJ, Griebel JJ, Kim ET, Yoon H, Simmonds AG, Ji HJ, et al. The use of elemental sulfur as an alternative feedstock for polymeric materials. Nat Chem 2013;5:518.
[8] Morsi MA, Rajeh A, Al-Muntaser AA. Reinforcement of the optical, thermal and electrical properties of PEO based on MWCNTs/Au hybrid fillers: nanodielectric materials for organoelectronic devices. Compos B Eng 2019;173:106957. https://doi.org/10.1016/j.compositesb.2019.106957.
[9] Zhu P, Xie X, Sun X, Soto MA. Distributed modular temperature-strain sensor based on optical fiber embedded in laminated composites. Compos B Eng 2019;168:267–73. https://doi.org/10.1016/j.compositesb.2018.12.078.
[10] Wang C, Chen J, Talavage T, Irudayaraj J. Gold Nanorod/Fe3O4 nanoparticle "nano-pearl- necklaces" for simultaneous targeting, dual-mode imaging, and photothermal ablation of cancer cells. Angew Chem Int Ed 2009;48:2759–63. https://doi.org/10.1002/anie.200805282.
[11] Liu J, Nakamura Y, Ogura T, Shibasaki Y, Ando S, Ueda M. Optically transparent sulfur-containing polyimide− TiO2 nanocomposite films with high refractive index and negative pattern formation from poly (amic acid)− TiO2 nanocomposite film. Chem Mater 2008;20:273–81.
[12] Ni M, Chen G, Wang Y, Peng H, Liao Y, Xie X. Holographic polymer nanocomposites with ordered structures and improved electro-optical performance by doping POSS. Compos B Eng 2019;174:107045. https://doi.org/10.1016/j.compositesb.2019.107045.
[13] Sun Z, Yan Z, Yue K, Li A, Qian L. Novel high-performance electromagnetic absorber based on Nitrogen/Boron co-doped reduced graphene oxide. Compos B Eng 2020;196:108132. https://doi.org/10.1016/j.compositesb.2020.108132.

[14] Yin L, Doyhamboure–Fouquet J, Tian X, Li D. Design and characterization of radar absorbing structure based on gradient-refractive-index metamaterials. Compos B Eng 2018;132:178–87. https://doi.org/10.1016/j.compositesb.2017.09.003.

[15] Abouhaswa AS, Rammah YS, Sayyed MI, Tekin HO. Synthesis, structure, optical and gamma radiation shielding properties of B2O3-PbO2-Bi2O3 glasses. Compos B Eng 2019;172:218–25. https://doi.org/10.1016/j.compositesb.2019.05.040.

[16] Zhang D, Sun D, Wen Q, Wen T, Kolodzey J, Zhang H. Tuning the optical modulation of wideband terahertz waves by the gate voltage of graphene field effect transistors. Compos B Eng 2016;89:54–9. https://doi.org/10.1016/j.compositesb.2015.10.049.

[17] Zhang S, Jiang R, Xie YM, Ruan Q, Yang B, Wang J, et al. Colloidal moderate-refractive-index Cu2O nanospheres as visible-region nanoantennas with electromagnetic resonance and directional light-scattering properties. Adv Mater 2015;27:7432–9. https://doi.org/10.1002/adma.201502917.

[18] Barreda ÁI, Saleh H, Litman A, González F, Geffrin J-M, Moreno F. On the scattering directionality of a dielectric particle dimer of High Refractive Index. Sci Rep 2018;8:1–12.

[19] Xiao S, Mei H, Han D, Cheng L. Sandwich-like SiCnw/C/Si3N4 porous layered composite for full X-band electromagnetic wave absorption at elevated temperature. Compos B Eng 2020;183:107629. https://doi.org/10.1016/j.compositesb.2019.107629.

[20] Nie R-P, Lei J, Jia L-C, Chen C, Xu L, Li Y, et al. Significantly improved high-temperature performance of polymer dielectric via building nanosheets and confined space. Compos B Eng 2020;196:108108. https://doi.org/10.1016/j.compositesb.2020.108108.

[21] Ko Y, Yoon H, Kwon S, Lee H, Park M, Jeon I, et al. Elastomeric high-κ composites of low dielectric loss tangent: experiment and simulation. Compos B Eng 2020;201:108337. https://doi.org/10.1016/j.compositesb.2020.108337.

[22] Zhang M, Xu P, Peng H, Qin F. A rational design of core-shell-satellite structured BaTiO3 fillers for epoxy-based composites with enhanced microwave dielectric constant and low loss. Compos B Eng 2021;215:108764. https://doi.org/10.1016/j.compositesb.2021.108764.

[23] Kleine TS, Nguyen NA, Anderson LE, Namnabat S, Lavilla EA, Showghi SA, et al. High refractive index copolymers with improved thermomechanical properties via the inverse vulcanization of sulfur and 1,3,5-triisopropenylbenzene. ACS Macro Lett 2016;5:1152–6. https://doi.org/10.1021/acsmacrolett.6b00602.

[24] Anderson LE, Kleine TS, Zhang Y, Phan DD, Namnabat S, LaVilla EA, et al. Chalcogenide hybrid inorganic/organic polymers: ultrahigh refractive index polymers for infrared imaging. ACS Macro Lett 2017;6:500–4.

[25] Griebel JJ, Namnabat S, Kim ET, Himmelhuber R, Moronta DH, Chung WJ, et al. New infrared transmitting material via inverse vulcanization of elemental sulfur to prepare high refractive index polymers. Adv Mater 2014;26:3014–8. https://doi.org/10.1002/adma.201305607.

[26] Olshavsky MA, Allcock HR. Polyphosphazenes with high refractive indices: synthesis, characterization, and optical properties. Macromolecules 1995;28:6188–97. https://doi.org/10.1021/ma00122a028.

[27] Shobha HK, Johnson H, Sankarapandian M, Kim YS, Rangarajan P, Baird DG, et al. Synthesis of high refractive-index melt-stable aromatic polyphosphonates. J Polym Sci Part A Polym Chem 2001;39:2904–10.

[28] Goosey E. Brominated flame retardants: their potential impacts and routes into the environment. 2006. Circuit World.

[29] Häußler M, Lam JWY, Qin A, Tse KKC, Li MKS, Liu J, et al. Metallized hyperbranched polydiyne: a photonic material with a large refractive index tunability and a spin-coatable catalyst for facile fabrication of carbon nanotubes. Chem Commun 2007:2584–6.

[30] Manners I. Polyferrocenylsilanes: metallopolymers for electronic and photonic applications. J Opt A Pure Appl Opt 2002;4:S221.

[31] Paquet C, Cyr PW, Kumacheva E, Manners I. Polyferrocenes: metallopolymers with tunable and high refractive indices. Chem Commun 2004;234–5.

[32] Boyd DA, Nguyen VQ, McClain CC, Kung FH, Baker CC, Myers JD, et al. Optical properties of a sulfur-rich organically modified chalcogenide polymer synthesized via inverse vulcanization and containing an organometallic comonomer. ACS Macro Lett 2019;8:113–6. https://doi.org/10.1021/acsmacrolett.8b00923.

[33] Kubo S, Diaz A, Tang Y, Mayer TS, Khoo IC, Mallouk TE. Tunability of the refractive index of gold nanoparticle dispersions. Nano Lett 2007;7:3418–23. https://doi.org/10.1021/nl071893x.

[34] Chen Q, Lin MR, Lee JE, Zhang QM, Yin S. Nanocomposites with very large electro-optic effect and widely tunable refractive index. Appl Phys Lett 2006;89:141121. https://doi.org/10.1063/1.2360183.

[35] Mahendia S, Kumar Tomar A, Goyal PK, Kumar S. Tuning of refractive index of poly(vinyl alcohol): effect of embedding Cu and Ag nanoparticles. J Appl Phys 2013;113:073103. https://doi.org/10.1063/1.4792473.

[36] Lü C, Yang B. High refractive index organic-inorganic nanocomposites: design, synthesis and application. J Mater Chem 2009;19:2884–901. https://doi.org/10.1039/b816254a.

[37] Tao P, Li Y, Rungta A, Viswanath A, Gao J, Benicewicz BC, et al. TiO2 nanocomposites with high refractive index and transparency. J Mater Chem 2011;21:18623. https://doi.org/10.1039/c1jm13093e.

[38] Li Y, Zhu J, Wei S, Ryu J, Sun L, Guo Z. Poly (propylene)/graphene nanoplatelet nanocomposites: melt rheological behavior and thermal, electrical, and electronic properties. Macromol Chem Phys 2011;212:1951–9.

[39] Zhu J, Wei S, Ryu J, Budhathoki M, Liang G, Guo Z. In situ stabilized carbon nanofiber (CNF) reinforced epoxy nanocomposites. J Mater Chem 2010;20:4937–48.

[40] Meneghetti P, Qutubuddin S. Synthesis, thermal properties and applications of polymer-clay nanocomposites. Thermochim Acta 2006;442:74–7.

[41] Islam MD, Liu S, Boyd DA, Zhong Y, Nahid MM, Henry R, et al. Enhanced mid-wavelength infrared refractive index of organically modified chalcogenide (ORMOCHALC) polymer nanocomposites with thermomechanical stability. Opt Mater (Amst) 2020;108:110197. https://doi.org/10.1016/j.optmat.2020.110197.

[42] Singh J, Rathi A, Rawat M, Kumar V, Kim K-H. The effect of manganese doping on structural, optical, and photocatalytic activity of zinc oxide nanoparticles. Compos B Eng 2019;166:361–70. https://doi.org/10.1016/j.compositesb.2018.12.006.

[43] Camenzind A, Schweizer T, Sztucki M, Pratsinis SE. Structure & strength of silica-PDMS nanocomposites. Polymer (Guildf) 2010;51:1796–804. https://doi.org/10.1016/j.polymer.2010.02.030.

[44] Hutchinson NJ, Coquil T, Navid A, Pilon L. Effective optical properties of highly ordered mesoporous thin films. Thin Solid Films 2010;518:2141–6.

[45] Ravindren R, Mondal S, Nath K, Das NC. Prediction of electrical conductivity, double percolation limit and electromagnetic interference shielding effectiveness of copper nanowire filled flexible polymer blend nanocomposites. Compos B Eng 2019;164:559–69. https://doi.org/10.1016/j.compositesb.2019.01.066.

[46] Puranik SM, Kumbharkhane AC, Mehrotra SC. The static permittivity of binary mixtures using an improved Bruggeman model. J Mol Liq 1994;59:173–7.

[47] Robertson WM, Arjavalingam G, Shinde SL. Microwave dielectric measurements of zirconia-alumina ceramic composites: a test of the Clausius–Mossotti mixture equations. J Appl Phys 1991;70:7648–50.

[48] Blanchard C, Portí JA, Morente JA, Salinas A, Navarro EA. Determination of the effective permittivity of dielectric mixtures with the transmission line matrix method. J Appl Phys 2007;102:64101.

[49] Peiponen K-E, Gornov E. Description of Wiener bounds of multicomponent composites by barycentric coordinates. Opt Lett 2006;31:2202–4.

[50] Jeong D-Y, Wang YK, Huang M, Zhang QM, Kavarnos GJ, Bauer F. Electro-optical response of the ferroelectric relaxor poly (vinylidene fluoride-trifluoroethylene-chlorofluoroethylene) terpolymer. J Appl Phys 2004;96:316–9.

[51] Chandler-Horowitz D, Amirtharaj PM. High-accuracy, midinfrared (450 cm− 1⩽ ω⩽ 4000 cm− 1) refractive index values of silicon. J Appl Phys 2005;97:123526.

[52] Chandrasekharan R, Masel RI, Shannon MA. Experimental technique using FTIR to estimate IR optical properties at variable temperatures: application to PMDA-ODA polyimide thin films from 100 to 380 °c. Rev Sci Instrum 2007;78. https://doi.org/10.1063/1.2736337.

[53] Edwards DF, Ochoa E. Infrared refractive index of silicon. Appl Opt 1980;19:4130–1.

[54] Smith DR, Loewenstein EV. Optical constants of far infrared materials 3: plastics. Appl Opt 1975;14:1335. https://doi.org/10.1364/ao.14.001335.

[55] Loewenstein EV, Smith DR. Optical constants of far infrared materials I: analysis of channeled spectra and application to mylar. Appl Opt 1971;10:577. https://doi.org/10.1364/ao.10.000577.

[56] Perot A, Fabry C. On the application of interference phenomena to the solution of various problems of spectroscopy and metrology. Astrophys J 1899;9:87.

[57] Wave Optics Module User's Guide. COMSOL Multiphysics® 1998:70–116.

[58] Böhm J, Haußelt J, Henzi P, Litfin K, Hanemann T. Tuning the refractive index of polymers for polymer waveguides using nanoscaled ceramics or organic dyes. Adv Eng Mater 2004;6:52–7. https://doi.org/10.1002/adem.200300542.

[59] Liu JG, Ueda M. High refractive index polymers: fundamental research and practical applications. J Mater Chem 2009;19:8907–19. https://doi.org/10.1039/b909690f.

[60] Griebel JJ, Nguyen NA, Astashkin AV, Glass RS, Mackay ME, Char K, et al. Preparation of dynamic covalent polymers via inverse vulcanization of elemental sulfur. ACS Macro Lett 2014;3:1258–61.

[61] Boyd DA, Baker CC, Myers JD, Nguyen VQ, Drake GA, McClain CC, et al. ORMOCHALCs: organically modified chalcogenide polymers for infrared optics. Chem Commun 2017;53:259–62. https://doi.org/10.1039/C6CC08307B.

[62] Miles P. High transparency infrared materials. Opt Eng 1976;15:155451. https://doi.org/10.1117/12.7972019.

[63] Cai J, Miao YQ, Yu BZ, Ma P, Li L, Fan HM. Large-scale, facile transfer of oleic acid-stabilized iron oxide nanoparticles to the aqueous phase for biological applications. Langmuir 2017;33:1662–9. https://doi.org/10.1021/acs.langmuir.6b03360.

[64] Diez S, Hoefling A, Theato P, Pauer W. Mechanical and electrical properties of sulfur-containing polymeric materials prepared via inverse vulcanization. Polymers (Basel) 2017;9:1–16. https://doi.org/10.3390/polym9020059.

[65] Tang J, Brzozowski L, Barkhouse DAR, Wang X, Debnath R, Wolowiec R, et al. Quantum dot photovoltaics in the extreme quantum confinement regime: the surface-chemical origins of exceptional air-and light-stability. ACS Nano 2010;4:869–78.

[66] Zhang H, Hyun B-R, Wise FW, Robinson RD. A generic method for rational scalable synthesis of monodisperse metal sulfide nanocrystals. Nano Lett 2012;12:5856–60.

[67] Nagao D, Kinoshita T, Watanabe A, Konno M. Fabrication of highly refractive, transparent BaTiO3/poly (methyl methacrylate) composite films with high permittivities. Polym Int 2011;60:1180–4.

[68] Inkyo M, Tokunaga Y, Tahara T, Iwaki T, Iskandar F, Hogan CJ, et al. Beads mill-assisted synthesis of poly methyl methacrylate (PMMA)-TiO2 nanoparticle composites. Ind Eng Chem Res 2008;47:2597–604.

[69] Demir MM, Koynov K, Bubeck C, Park I, Lieberwirth I, Wegner G. Optical properties of composites of PMMA and surface-modified zincite nanoparticles 2007:1089–100. https://doi.org/10.1021/ma062184t.

[70] Mataki H, Yamaki S, Fukui T. Nanostructured organic/inorganic composites as transparent materials for optical components. Jpn J Appl Phys 2004;43:5819.

[71] Dirlam PT, Simmonds AG, Kleine TS, Nguyen NA, Anderson LE, Klever AO, et al. Inverse vulcanization of elemental sulfur with 1,4-diphenylbutadiyne for cathode materials in Li-S batteries. RSC Adv 2015;5:24718–22. https://doi.org/10.1039/c5ra01188d.

[72] Jenkins FA, White HE. Fundamentals of optics. Tata McGraw-Hill Education; 1937.
[73] Kassam S, Hodgkinson IJ, hong Wu Q, Cloughley SC. Light scattering from thin films with an oblique columnar structure and with granular inclusions. JOSA A 1995;12:2009–21.
[74] Mao P, Sun F, Yao H, Chen J, Zhao B, Xie B, et al. Extraction of light trapped due to total internal reflection using porous high refractive index nanoparticle films. Nanoscale 2014;6:8177–84.
[75] Mei K, Van Bladel J. Scattering by perfectly-conducting rectangular cylinders. IEEE Trans Antenn Propag 1963;11:185–92.
[76] Khattak HK, Bianucci P, Slepkov AD. Linking plasma formation in grapes to microwave resonances of aqueous dimers. Proc Natl Acad Sci Unit States Am 2019; 116:4000–5.